Supplementary information

Estimation of the droplet volume fraction from camera images:

The pressure field induced by the acoustic waves causes a vertical compression and thus a non-sphericity of the droplets placed below the pressure nodes. The camera observation plane being parallel to the direction of the acoustic waves (Fig. 1a), the 2D visualization of the droplets via the video snapshots could be regarded as an ellipse with a horizontal major radius α and a vertical minor radius β. Considering the vertical symmetry of the system, the radius in the third dimension of the droplet was assumed to be equal to α. Ellipse fitting performed on a number of video snapshots provided values for major and minor diameters (respectively 2α and 2β), from which the surface area (S) of the droplets could be estimated using *Equation S1*:

$$S = 4\pi\left(\frac{(\alpha^2)^{1.6} + 2\,(\alpha\beta)^{1.6}}{3}\right)^{\frac{1}{1.6}}$$

(S1)

The equivalent square diameter (δ^2), defined as the square diameter of a sphere that would have the same surface area as the ellipsoidal droplet, is a commonly used parameter in the study of levitating droplets[1] and was obtained via *Equation S2*:

$$\delta^2 = \frac{S}{\pi}$$

(S2)

Fig. 1b displays the results of the image processing for a droplet consisting of a CNC-only dispersion. Each point corresponds to an analysed snapshot, to which both a time stamp and an equivalent diameter were associated. The evolution of δ^2 with time followed a behaviour typical of levitating aqueous solid dispersions. Two stages were observed, respectively with white and red backgrounds on the graph (Fig. 1b): the droplet diameter first decreased then remained constant even though the drying was not complete.[2] While no information can be retrieved from the second stage (red), a parabolic fitting gives access to a δ^2 value over the whole first stage (white). A direct relationship then gives access to the droplet volume V (*Equation S3*):

$$V = \frac{4}{3}\pi\left(\frac{\delta^2}{4}\right)^{1.5}$$

(S3)

Finally, the volume fractions (φ) during the first stage were obtained from the droplet volumes via *Equation S4*:[3]

$$\varphi = \frac{C_0\,V_0}{\rho\,V}$$

(S4)

where C_0 is the initial mass concentration of the examined nanoparticles in the droplet, V_0 is the initial volume of the droplet and ρ the density of the examined nanoparticles. As shown in Fig. 1b, the obtained range for a CNC dispersion covers volume fractions from 1% to about 60%. Some indicative error bars are displayed: they result from the propagation of the initial image processing error estimated from the pixel size of the snapshots, which explains why higher volume fractions and thus smaller droplets induce a larger error, and they also take errors on the initial droplet stabilization time and mass fraction into account. The amplitude of the error bars remains reasonable over a wide range.
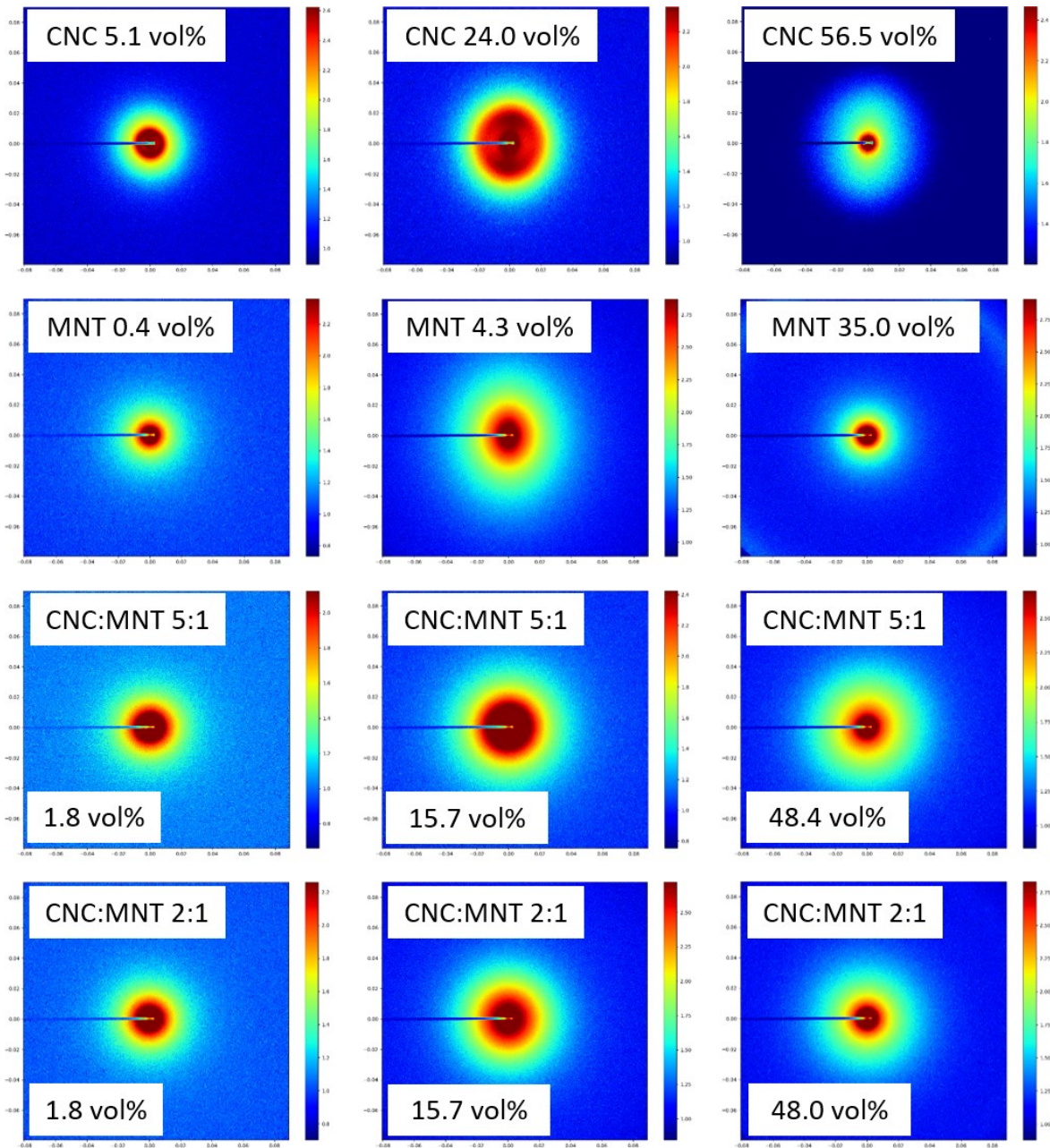
Fig. S1: 2D scattering patterns. 2D scattering patterns obtained at representative stages of their temporal evolution, displayed with increasing volume fractions from left to right (see insets).
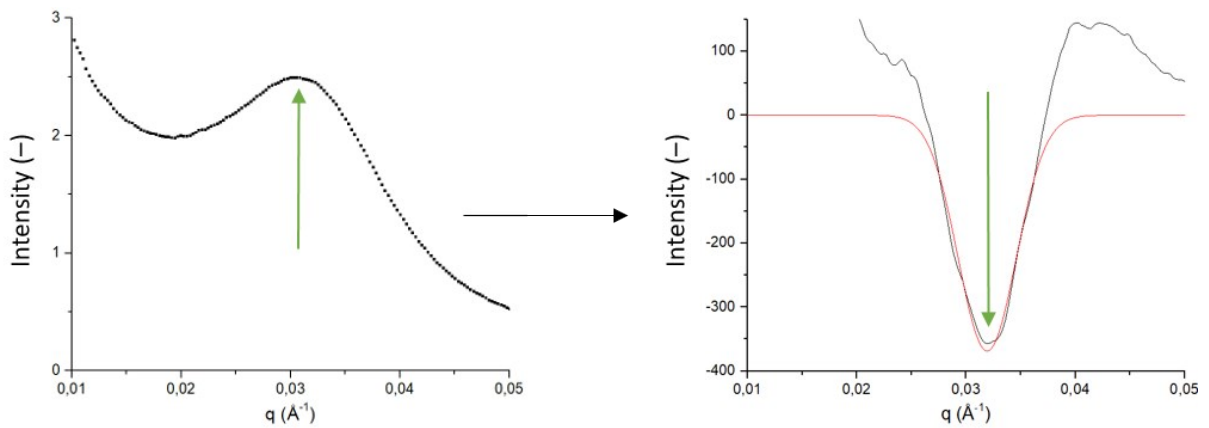
Fig. S2: Peak centre determination. Estimation of the CNC structural peak centres from the SAXS curves (left), highlighted by the arrows, by Gaussian fitting the smoothed second derivative of the signal (right).

CNC particle dimensions determined by Atomic Force Microscopy (AFM):

The CNC particles were observed using AFM as shown in Fig. S2. The characteristic dimensions of the nanorods could then be extracted from the obtained micrographs. Due to the cross-section of the CNC particles being widely considered rectangular,[4] we will further on refer to the shorter dimension of this rectangle as the thickness, and to its longer dimension as the width. Fig. S2 shows the distribution of thicknesses and lengths obtained from the measurement of 100 particles on several micrographs. The average thickness was found to be equal to 43 ± 13 Å, while the average length was 1540 ± 440 Å. The obtained average values are in line with what is commonly found in the literature.[5,6]
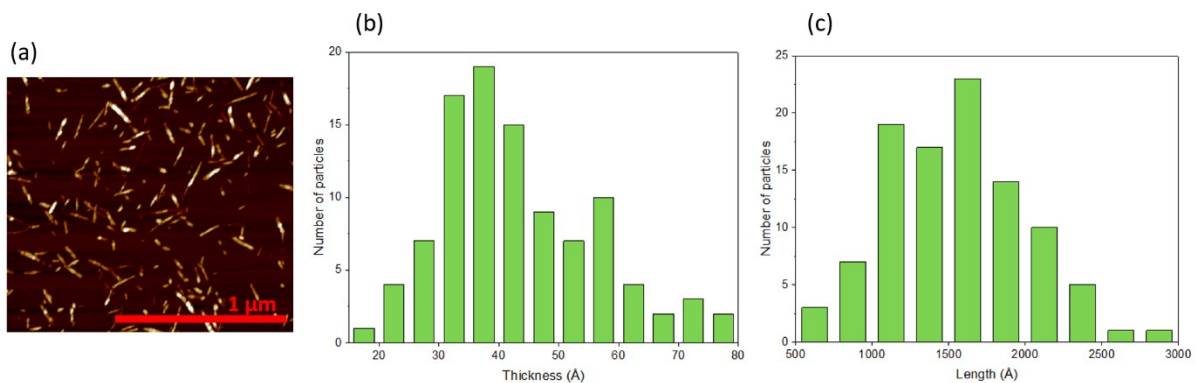

Fig. S3: CNC particle dimensions by AFM imaging. (a) Cellulose nanocrystals imaged by Atomic Force Microscopy (AFM). Distribution of (b) particle diameters and; (c) lengths, based on the measurement of 100 CNC particles observed in AFM micrographs.
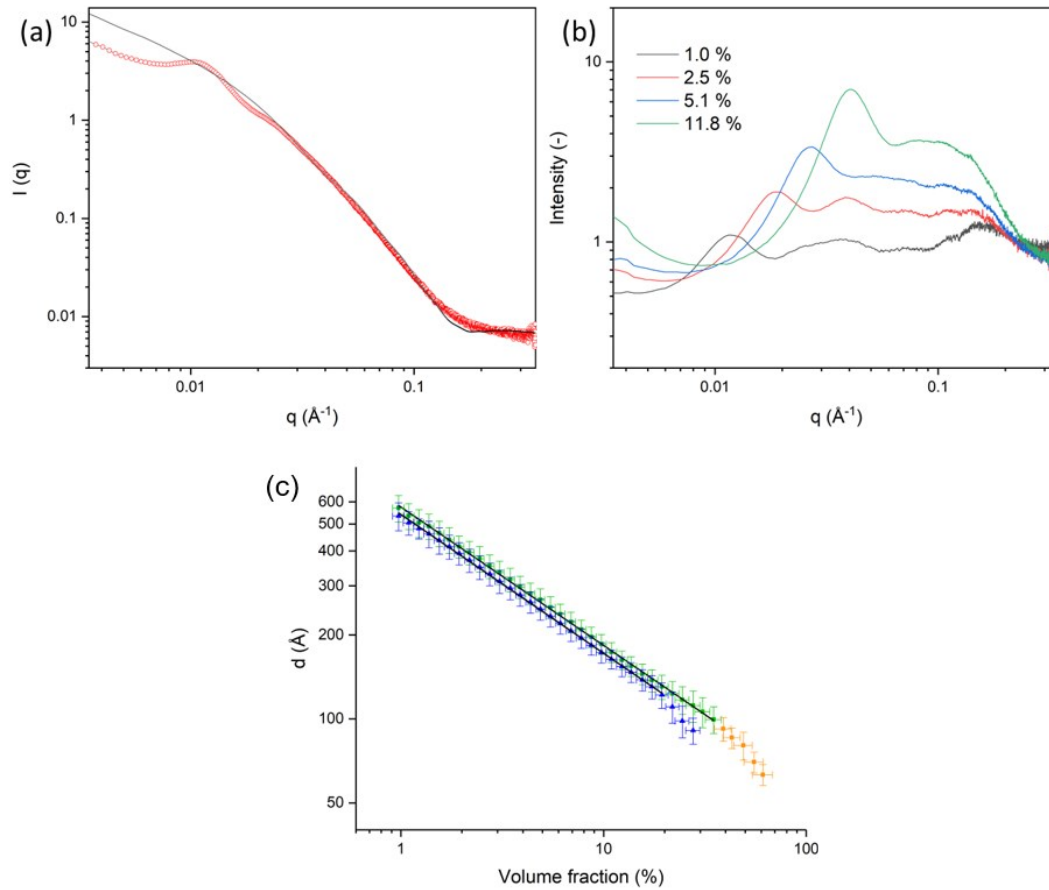
Fig. S4: CNC form and structure factors. (a) SAXS pattern of CNC system with a volume fraction of 1.0 % (red marker) and the fitted form factor (black line). (b) Structure factor extracted by dividing the experimental SAXS pattern by the fitted form factor. (c) Comparison of the power-law scalings obtained by peak centre analysis of the structure factor (blue triangles) and of the intensity curves (green and orange squares, see Fig. 2a in the main manuscript).

Table S1: Scaling factors of the broad peak model. Summary of the scaling factors A and B obtained with broad peak model fitting throughout the study.

| Dispersion mixture	Volume Fraction (%)	Low-q power-law scaling factor, A	Lorentzian scaling factor, B
CNC	24.0 ± 1.9	$5.7 \ 10^{-5} \pm 3 \ 10^{-6}$	$7.5 \ 10^{-1} \pm 4 \ 10^{-2}$
	32.0 ± 2.8	$1.8 \ 10^{-4} \pm 9 \ 10^{-6}$	$6.5 \ 10^{-1} \pm 4 \ 10^{-2}$
	35.7 ± 3.2	$3.2 \ 10^{-4} \pm 2 \ 10^{-5}$	$4.5 \ 10^{-1} \pm 2 \ 10^{-2}$
	56.5 ± 6.2	$3.5 \ 10^{-4} \pm 2 \ 10^{-5}$	$1.2 \ 10^{-1} \pm 6 \ 10^{-3}$
CNC:MNT = 5:1	15.7 ± 0.3	$3.9 \ 10^{-4} \pm 2 \ 10^{-5}$	$1.9 \ 10^{0} \pm 9 \ 10^{-2}$
	32.4 ± 0.9	$6.0 \ 10^{-4} \pm 3 \ 10^{-5}$	$7.6 \ 10^{-1} \pm 4 \ 10^{-2}$
	48.4 ± 1.4	$3.6 \ 10^{-4} \pm 2 \ 10^{-5}$	$5.6 \ 10^{-1} \pm 3 \ 10^{-2}$
CNC:MNT = 2:1	15.7 ± 0.8	$6.6 \ 10^{-4} \pm 3 \ 10^{-5}$	$1.4 \ 10^{0} \pm 7 \ 10^{-2}$
	32.4 ± 2.2	$5.6 \ 10^{-4} \pm 3 \ 10^{-5}$	$4.9 \ 10^{-1} \pm 2 \ 10^{-2}$
	48.0 ± 3.4	$5.0 \ 10^{-4} \pm 3 \ 10^{-5}$	$1.4 \ 10^{-1} \pm 7 \ 10^{-3}$
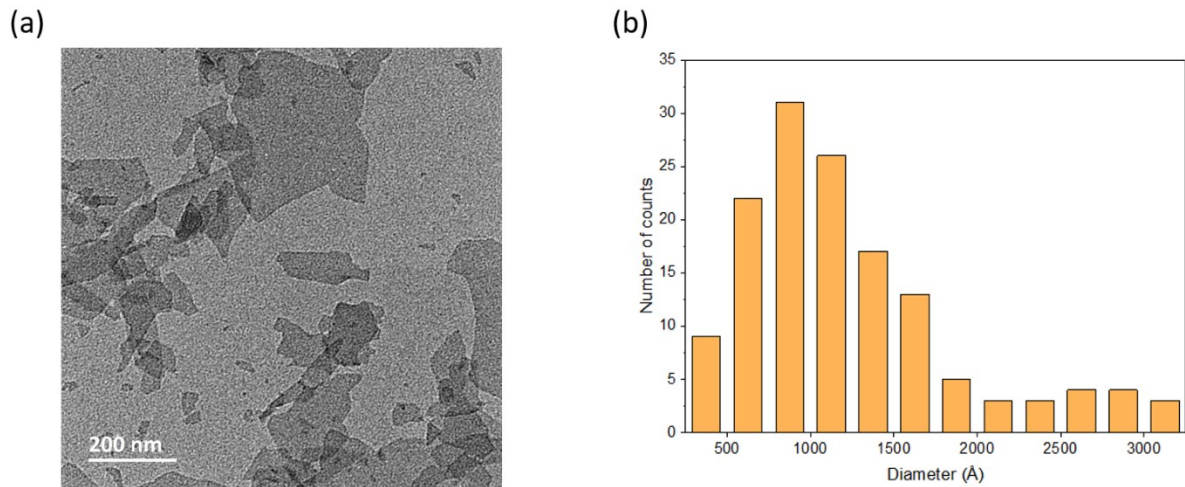
Fig. S5: MNT platelet size distribution via TEM imaging. (a) Montmorillonite platelets imaged by Transmission Electron Microscopy (TEM). (b) Distribution of platelet diameter based on the measurement of 70 MNT platelets observed in TEM images. Given the wide variety of shapes, each platelet dimension was measured in two directions.
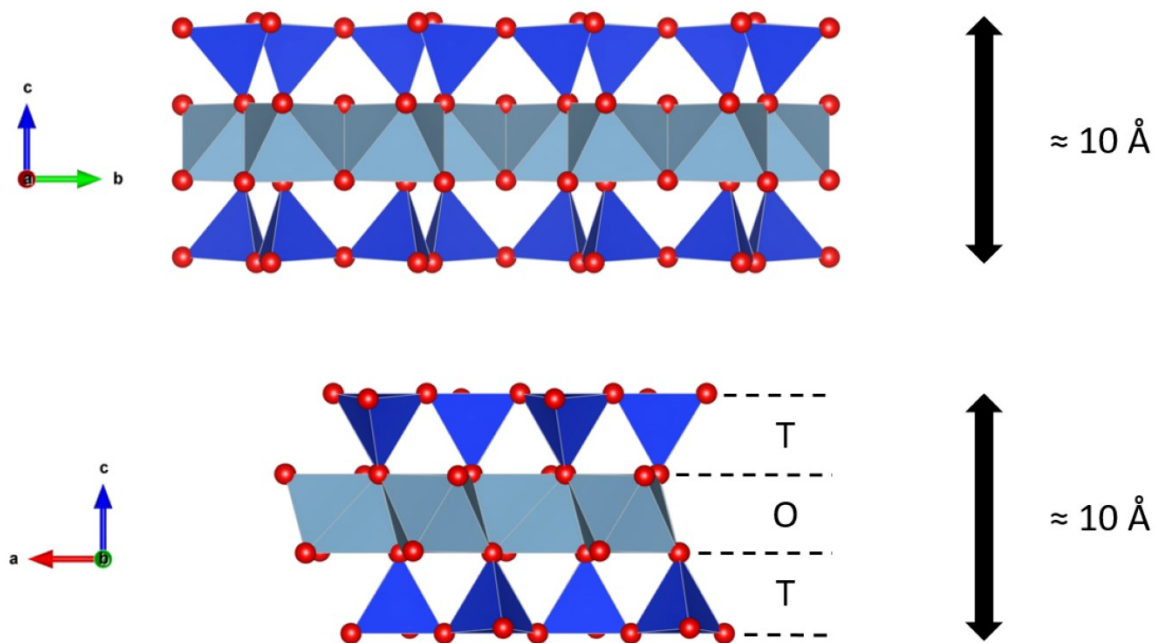

Fig. S6: Crystal structure of MNT. Visualization of the three polyhedral layers (T-O-T: tetrahedral-octahedral-tetrahedral) composing a MNT platelet (the c direction corresponds to the platelet thickness). The structure visualization was generated using the VESTA software and lattice parameters found in Viani et al.[7]
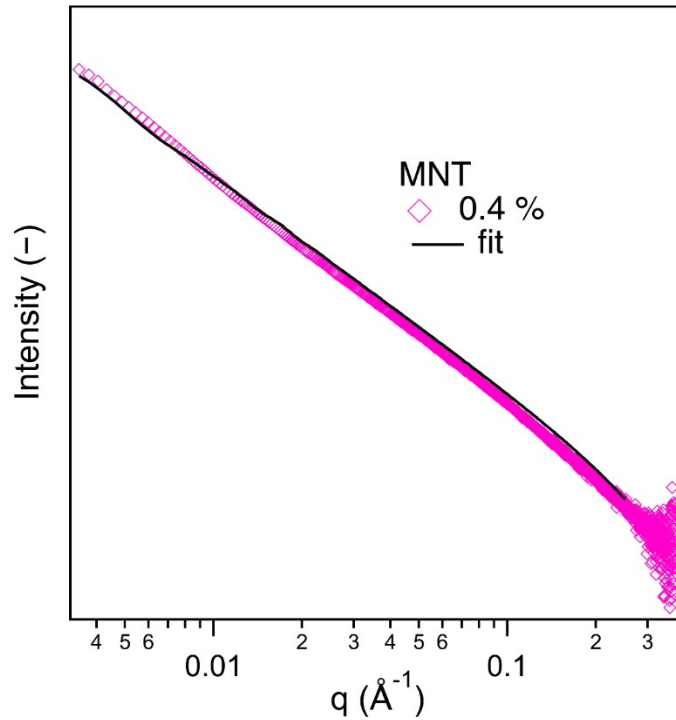
Fig. S7: Parallelepiped fitting of MNT SAXS pattern. SAXS curve corresponding to a MNT droplet with a volume fraction of 0.4 %, fitted with a parallelepiped model (the obtained χ^2 = 0.04 confirms the accuracy of the fit).
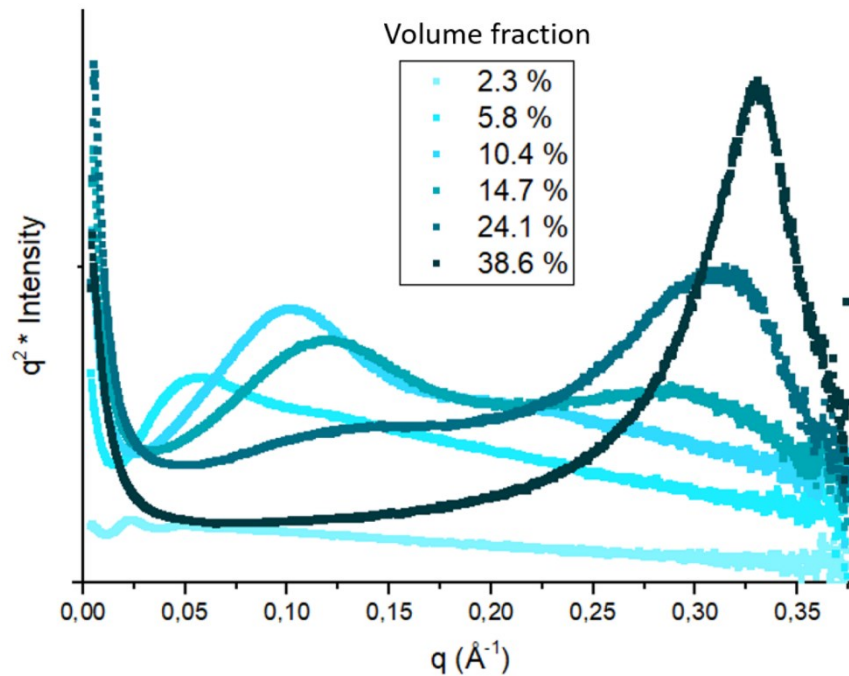

Fig. S8: Kratky visualization of MNT droplet SAXS data at various evaporation stages. Selection of SAXS curves corresponding to various stages of the evaporation of a MNT aqueous droplet, plotted in Kratky view to enhance the presence of a diffuse peak (q < 0.15 Å^{-1}) at intermediate volume fractions and a correlation peak (q > 0.30 Å^{-1}) at higher volume fractions.

References

1   C. K. Law, T. Y. Xiong and C. Wang, *Int. J. Heat Mass Transf.*, 1987, **30**, 1435–1443.

2   A. L. Yarin, G. Brenn, O. Kastner and C. Tropea, *Phys. Fluids*, 2002, **14**, 2289–2298.

3   M. Agthe, T. S. Plivelic, A. M. Labrador, L. Bergström and G. Salazar-Alvarez, *Nano Lett.*, 2016, **16**, 6838–6843.

4   F. Cherhal, F. Cousin and I. Capron, *Langmuir*, 2015, **31**, 5596–5602.

5   R. J. Moon, A. Martini, J. Nairn, J. Simonsen and J. Youngblood, *Chem. Soc. Rev.*, 2011, **40**, 3941–3994.

6   C. Honorato-Rios, C. Lehr, C. Schütz, R. Sanctuary, M. A. Osipov, J. Baller and J. P. F. Lagerwall, *NPG Asia Mater.*, 2018, **10**, 455–465.

7   A. Viani, A. F. Gualtieri and G. Artioli, *Am. Mineral.*, 2002, **87**, 966–975.